

ARTICLE OPEN

Topological characterizations of an extended Su–Schrieffer–Heeger model

Dizhou Xie¹, Wei Gou¹, Teng Xiao¹, Bryce Gadway² and Bo Yan^{1,3}

The Su–Schrieffer–Heeger (SSH) model perhaps is the easiest and the most basic model for topological excitations. Many variations and extensions of the SSH model have been proposed and explored to better understand both fundamental and novel aspects of topological physics. The SSH4 model has been proposed theoretically as an extended SSH model with higher dimension (the internal dimension changes from two to four). It has been proposed that the winding number in this system can be determined through a higher-dimensional extension of the mean chiral displacement measurement, however, this has not yet been verified in experiment. Here, we report the realization of this model with ultracold atoms in a momentum lattice. We verify the winding number through measurement of the mean chiral displacement in a system with higher internal dimension, we map out the topological phase transition in this system, and we confirm the topological edge state by observation of the quench dynamics when atoms are initially prepared at the system boundary.

npj Quantum Information (2019)5:1; https://doi.org/10.1038/s41534-019-0159-6

INTRODUCTION

Topological phases represent an exotic form of matter with geometrical origins. These phases can emerge without any symmetry breaking, which conflicts with the traditional Ginzburg–Landau paradigm. The topological phase is characterized by global properties rather than a local order, making it very robust to certain local perturbations; this topological robustness makes emergent topological excitations a promising candidate for quantum computing. Since the discovery of topological phases in the 1980s, comprehensive studies both in theory and experiment have been carried out to create, classify, and comprehend these exotic phases. Various systems across a range of platforms have been engineered to show topological properties, such as the solid, ^{1,2} photonic, ^{3,4} atomic, ^{5–9} acoustic, ^{10,11} and electronic ^{12,13} systems.

The ultracold atom system provides a powerful tool to study the exotic topological phases, because all the degrees of freedom are precisely controlled. Using optical lattices formed by laser interference, some topological models that are hard to study in other quantum systems can be realized in ultracold atom experiments, such as the famous Haldane model. 14 The band structure of the lattice can be engineered by choosing different lattice geometries (such as triangular, 15 kagome 16) or different energy bands, 17,18 and this approach of band structure engineering has been essential for introducing topological properties in a cold atom setting. Spin-orbit coupling (SOC) and artificial gauge fields can also be synthesized using light-atom coupling, 19they have been very important for studying the topological insulators. One important advantage of ultracold atom systems is the natural ability to study dynamical processes, 22,23 which is nearly impossible for other systems such as electronic materials. By suddenly quenching a system into the topological phase of a Hamiltonian, the resulting dynamical processes provide rich information, and can reveal the underlying topology of the system.

Among the wide variety of topological models, the Su–Schrieffer–Heeger (SSH) model is the most basic and one of the most important models in describing band topology in condensed matter physics.^{24–28} In order to study additional topological physics, various extended models have been proposed. By adding a periodic modulation to the tunneling or the on-site energy, one can study the driven SSH model.^{11,29,30} By adding long-range tunnelings between different sites, such as the next nearest-neighbor tunneling, one can study the long-range hopping SSH model.^{31,32} By extending the one-dimensional model to two chains, one can study the Creutz ladder model.^{33,34}

One direct extension of the SSH model is the so-called SSH4 model.³⁵ By changing the site period of the unit cell from two to four, one can transform the standard SSH model into the considerably richer SSH4 model. As shown in Fig. 1a, the tunneling rates between pairs of sites repeat every four lattice sites, and we label the fundamental tunneling terms as $\{t_a, t_b, t_c, t_d\}$. We additionally label the sublattice site positions within each unit cell as $\{A_1, B_1, A_2, B_2\}$. In the situation where $t_a = t_c$ and $t_b = t_{dt}$, the SSH4 model reduces to the common SSH model. For a SSH4 model with infinite sites, the topological phase is determined by the tunneling ratio $\gamma = bd/ac$. If $\gamma > 1$, it is topologically nontrivial and can hold topological, zero-energy edge states. If y < 1, it is topologically trivial and no edge state exists. In Fig. 1b, we plot the eigenenergy of the SSH4 system with six unit cells versus 1/y with six unit cells. Here, we choose $t_b = t_c = t_d = 2\pi \times 1$ kHz and vary t_a . There exist states at zero energy when 1/y < 1, and these states, the topological edge states, can be shown to exist at the boundary of the system. Figure 1c shows one typical population distribution

¹Zhejiang Province Key Laboratory of Quantum Technology and Device, Department of Physics and State Key Laboratory of Modern Optical Instrumentation, Zhejiang University, 310027 Hangzhou, Zhejiang, China; ²Department of Physics, University of Illinois at Urbana-Champaign, Urbana, IL 61801-3080, USA and ³Collaborative Innovation Centre of Advanced Microstructures, Nanjing University, 210093 Nanjing, China Correspondence: Bo Yan (yanbohang@zju.edu.cn)

Received: 12 December 2018 Accepted: 7 May 2019

Published online: 30 May 2019





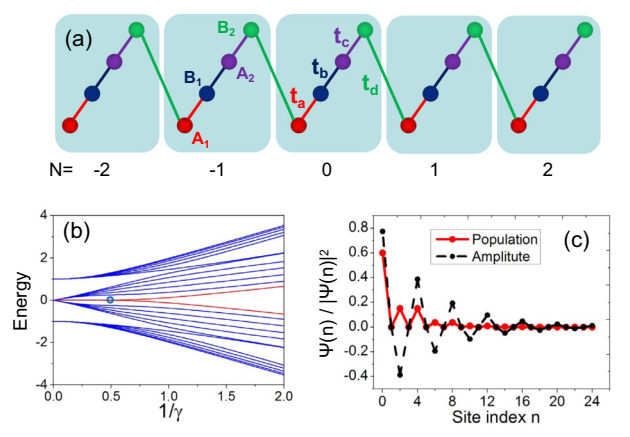


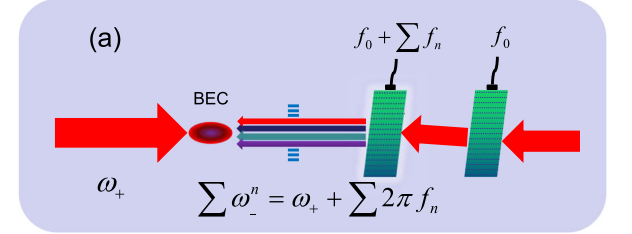
Fig. 1 a The diagrammatic sketch of the SSH4 model. Tunneling terms are periodic with a unit cell of four sites. **b** The eigenenergy of each eigenstate for different γ with the SSH4 model for N=6. $t_b=t_c=t_d=2\pi\times 1$ kHz, and t_a varies. The red lines show that there are eigenstates with zero energy when $1/\gamma<1$, which correspond to the existence of topological edge states. When $1/\gamma>1$, there are no zero-energy eigenstates. For a large system (large N number), a sharp phase transition happens at $\gamma=1$. **c** The probability amplitude and the population distribution for an edge state when $1/\gamma=0.5$, as circled in **b**

for the edge state when $1/\gamma = 1/2$. The population is mainly distributed within the first unit cell.

One of the interesting features of the SSH4 model lies in the much wider parameter space. The larger parameter space of the SSH4 model with an enhanced unit cell is useful for studying topological properties with higher dimensions^{5,36,37} and potentially also a higher winding number.³⁸ When periodical driving is applied to the SSH4 system, an effectively higher-dimensional quantum model can be realized. Reference proposed an example of forming a discrete-time quantum walk with effectively four dimensions by driving the SSH4 model. An interesting feature of the SSH4 model relates to the methods for detecting the winding number in such systems. The mean chiral displacement has been proposed and experimentally verified as an observable that reveals the winding number in the standard SSH model.^{8,39} Reference³⁵ provides a generalized description of how this observable can be extended to higher-dimensional systems, however, it has yet to be verified in experiment. In this paper, we have realized the higher-dimensional (in the internal dimension of the unit cell) SSH4 model with ultracold atoms in momentum space, which would be quite difficult to engineer in real space. We have verified the utility of the mean chiral displacement measurement in this higher-dimensional model, using it to map out the topological phases of the SSH4 system.

RESULTS

In experiment, we use ultracold atoms in a momentum lattice to realize the SSH4 model. Such quantum simulator is a versatile platform for studying topological models. We first produce a 87 Rb Bose–Einstein condensate (BEC) in a crossed dipole trap. The BEC contains about 6×10^4 atoms, and the trap frequencies are $\sim 2\pi\times(90, 90, 90)$ Hz. We use an additional 1064-nm beam to Raman couple the different momentum states. As shown in Fig. 2a, the incoming beam (ω_+) passes through the atomic BEC and is then reflected back upon itself, in the antiparallel direction. It goes through two AOMs before again passing through the cloud of atoms. One AOM is driven by $f_0=100$ -MHz radio frequency (RF) and the +1 order is chosen, while for the second one, $f=f_0+\Sigma f_n$ and the -1 order is chosen. Atoms can absorb a photon from one direction (ω_+) and undergo stimulated emission of a photon into



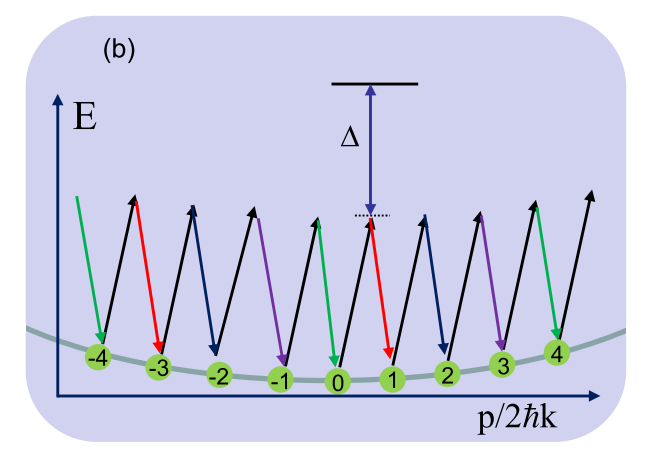


Fig. 2 a The experimental setup for multifrequency Raman coupling. The incoming Raman beam passes the BEC, then passes two AOMs, and finally propagates back to the BEC. One AOM is modulated with a frequency f_0 , and the other one is modulated with the multifrequency signal $f_0 + \sum f_n$. One AOM is operated in the positive first order. while the other is operated in the negative first order. So the two Raman beams on BEC differ in frequency by $\sum f_n$. **b** An illustration of the Raman processes driven by a pair of Raman beams

the opposite direction (ω_-) . Thus, a total two-photon recoil momentum $p_0=2\hbar k$ is transferred to the atom. As shown in Fig. 2b, each pair of the Raman beams $\{\omega_+\oplus\omega_-^n\}$ couple the momentum states from $\{np_0\}$ to $\{(n+1)p_0\}$. Hereafter, we label the momentum state with momentum np_0 as $|n\rangle$. The momentum states $\{...,-2,-1,0,1,2,...\}$ form an effective lattice structure in the momentum space. f_n is set to be $(2n+1)\times 4E_r$ ($E_r=h\times 2.03$ kHz) to resonantly couple different momentum states from $|n\rangle$ to $|n+1\rangle$. In our experiment, we detect the atomic distribution by suddenly turning off all of the laser beams and allowing atoms to fall in free space for 20 ms, such that atoms in different momentum states evolve to different positions. Then we take an absorption image and count the number of atoms in the different momentum states.

This Raman coupled momentum lattice structure can be described by a simple tight-binding model. With the rotating-wave approximation, the Hamiltonian is 42

$$H = \sum_{n} t_{n} [e^{i\phi_{n}} (|\hat{\psi}_{n+1}\rangle\langle\hat{\psi}_{n}| + H.c.)], \tag{1}$$

where ϕ_n are the relative phases for different tunnelings, which are determined by the relative phases between lasers with different frequencies. In our case, all these phases are set to be zero. t_n are the tunneling rates, determined by the Raman coupling strength of each Raman beam pair, $t_n = \Omega_+ \Omega_n / 4\Delta$. They can be adjusted by changing the laser intensity of each discrete frequency component. If the t_n are set to take different values for the alternating tunneling links, the Hamiltonian can be mapped to the standard SSH model. If t_n are set to be periodic over every four sites, this system realizes the SSH4 model.

For one-dimensional chiral models, the winding number v is an important topological invariant used to characterize the

topological phase. The number of edge states on each edge is $|\nu|$. It can be measured by detecting the phase of a particle across the Brillouin zone, ²⁴ and can also be measured with a quench dynamics. ³⁵ The mean chiral displacement was recently introduced to measure the winding number and has been conducted in the photonic system ³⁹ and cold atom system ⁸ for the SSH model, and it is quite insensitive to disorder. The mean chiral displacement is defined as

$$C(t) = \langle \Gamma m \rangle;$$
 (2)

which quantifies the relative shift between the projections of the state onto the eigenstates of the chiral operator Γ . Here \hat{m} is the unit cell operator. The dynamics of C(t) converge to the winding number v for the long-time dynamics for initial states beginning within one unit cell following 8,39

$$v = \operatorname{Tr}(\widehat{\Gamma m}); \tag{3}$$

For the SSH4 model, we can choose the unit cell basis $\{A_1, B_1, A_2, B_2\}$, so that the total mean chiral displacement operator takes the form $\widehat{\Gamma m} = diag(..., 1, -1, 1, -1, 2, -2, 2, -2, ...)$. At higher dimension, in order to use the mean chiral displacement to measure the winding number, we need to choose an orthogonal and complete basis of a given sublattice. In our case, we prepare the initial state at two orthogonal states (1,0,0,0) and (0,0,1,0), and measure the mean chiral displacement $C_1(t)$ and $C_3(t)$, respectively. Then we sum these two measures $C_{total}(t) = C_1(t) + C_3(t)$ to get the total mean chiral displacement, which converges to the winding number v at long evolution times.

Figure 3 shows the experimental results of the mean chiral displacement measurement. The RF driver of the AOM includes 24 discrete frequency teeth, so the unit cell number of this SSH4 model is N=6. The initial state is prepared within the central unit cell. By suddenly turning on the Raman couplings, the dynamics of the evolution is recorded and the $C_{total}(t) = C_1(t) + C_3(t)$ is extracted. To enter the different topological phases, we choose the tunneling about $t_a = t_c = t_d = 2\pi \times 1$ kHz, and vary the ratio t_b/t_a . The left inset shows $C_{total}(t)$ when $\gamma < 1$, it oscillates around zero. The right inset shows $C_{total}(t)$ when $\gamma > 1$, which rises up and then oscillates around one. The dynamics of $C_{total}(t)$ show completely different behaviors in these two regimes. The blue curves are the ideal numerical simulations according to Eq. (1), which capture the main features of the experimental data. We

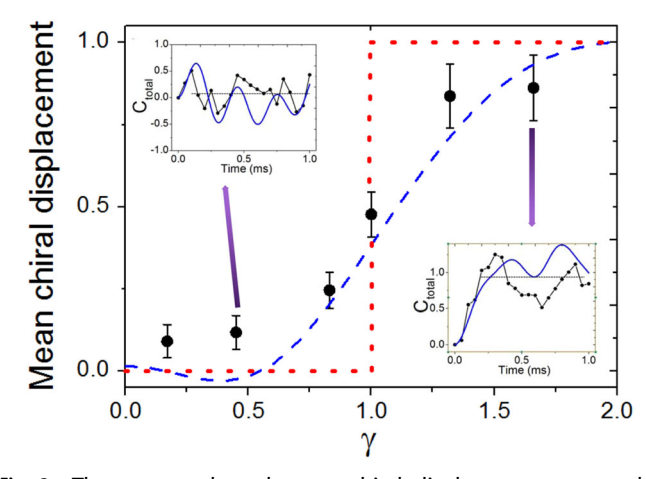


Fig. 3 The measured total mean chiral displacement versus the tunneling ratio γ . The black dots are experimental data. The blue dashed line is the theoretical simulation with N=6 unit cells. The red dashed line is the theoretical simulation with $N\to\infty$, where a sharp phase transition occurs at $\gamma=1$. The insets show the two data sets for $\gamma<1$ and $\gamma>1$, respectively. For these insets, the dots are the experimental data and blue lines are the simulations. Error bars are defined as the standard deviation

extract the averaged value and then plot it versus different γ , as shown in Fig. 3. The error bars of the data points mainly stem from uncertainty, due to the presence of a thermal fraction (about 10% of the total population in our experiments). The red curve is the theory prediction for an infinite number of unit cell $N \to \infty$. When N is a large number, the topological phase transition is sharp in the thermodynamic sense. The blue dashed curve is a numerical simulation with our experimental parameters for N=6, in which case, one finds a smooth transition between topologically trivial and topologically nontrivial phases. Our data agree with the theory quite well.

In addition to measuring the bulk topology through the mean chiral displacement, we also directly detect the boundary signatures of the topology through quench dynamics at the edge of our SSH4 model. Figure 4 shows the typical experimental results of edge guench dynamics. The BEC is prepared at the |0 > state, and then we turn on the Raman coupling and let the BEC evolve under the SSH4 Hamiltonian. The parameters are chosen as $t_a = t_c$ $= t_d = 2\pi \times 0.5$ kHz and $t_b = 2\pi \times 1$ kHz. Because $\gamma > 1$, the edge states should exist under these conditions. For Fig. 4a, b, the Raman beams are designed to couple the momentum states of $n = \{0, 1, 2, ..., 19\}$. So, the initial state is prepared at the edge, which is not exactly the eigenstate of the edge state, but has a big overlap with its wavefunction. In this case, we will expect the population to continuously remain at the $|0\rangle$ position. Figure 4a displays the experimental data. The different positions along the x direction relate to the different discrete momentum states, which are labeled at the top of the picture. The time step of our measurements is 50 μ s. We see that the population in the $|0\rangle$ state remains dominate over time, as expected. Figure 4b is the theoretical simulation with $t_a = t_c = t_d = 2\pi \times 0.5 \text{ kHz}$ and $t_b = 2\pi \times 1$ kHz. The experimental and theoretically simulated dynamics display good agreement. For initial preparations of a bulk state, the system shows distinct dynamical behavior. For Fig. 4c, d, the Raman coupling is designed to couple $n = \{-11, ..., -1,$ 0, 1, ..., 12} states, such that the initial BEC state is in the bulk. The population in $|0\rangle$ can be seen to nearly vanish, even at these relatively short times. Figure 4c is the experimental data and Fig. 4d is the theoretical simulation with $t_a = t_c = t_d = 2\pi \times 0.5$ kHz and $t_b = 2\pi \times 1$ kHz. Again, we find generally good qualitative agreement between theory and experiment in this case of bulk injection. For both the edge and bulk injection cases, we observe that the experiment and theory are in good agreement at short time, but begin to deviate at longer times. Some possible sources of this deviation, deserving future investigation, include Raman laser-phase noise, the expansion and separation of the momentum states, and atomic interactions.

DISCUSSION

To conclude, we have experimentally realized a new kind of extended SSH model, the SSH4 model, in a momentum lattice with ultracold atoms. We have measured the bulk topological properties of this system through quench dynamics. We have measured the winding number by means of the mean chiral displacement, and the phase transition is mapped out. We have found quite excellent agreement between the experimental data and the mean chiral displacement theory, which shows a robustness of this dynamical topological observable, even in the presence of effects limiting the long-time dynamics. We attribute this to the insensitivity of the mean chiral displacement to disorders as confirmed in refs. 8,39 Our result is the first experimental demonstration of the mean chiral displacement predicted at higher dimension. In addition to our measurements of the bulk topology, we confirm these results by directly observing evidence for topological boundary states at the edge of our SSH4 lattice.



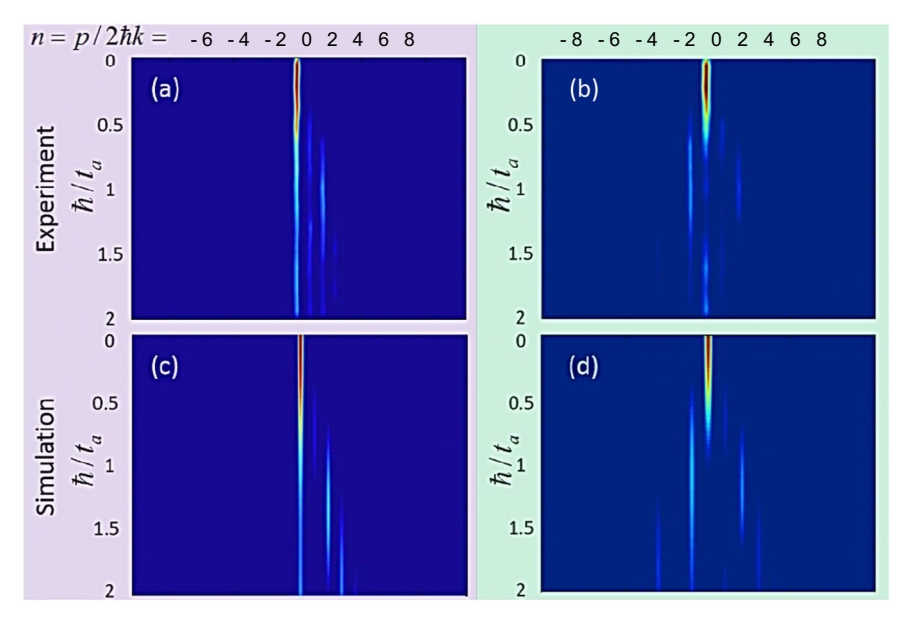


Fig. 4 Quench dynamics of the SSH4 model. a The initial state is prepared at the edge. b The theoretical simulations for the edge dynamics. c The initial state is prepared within the bulk. d The theoretical simulations for the bulk state. When the initial state is prepared at the edge, the population at the zero site is always dominant, while for the case of bulk injection, the zero-site population vanishes even for short quench durations. These quench dynamics confirm the boundary correspondence of the bulk topology observed in Fig. 3

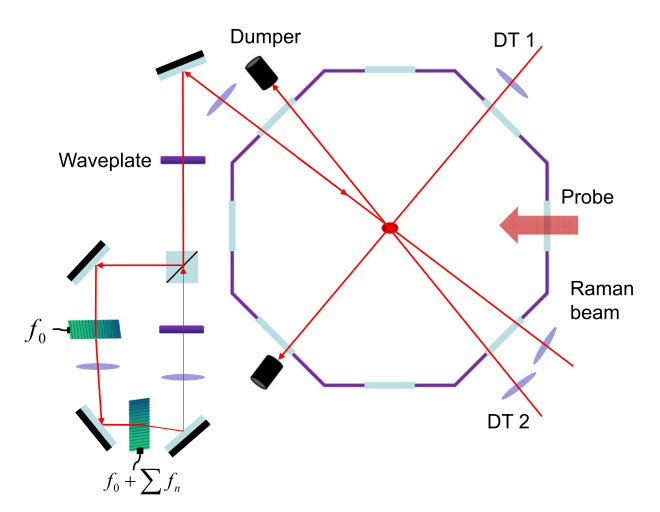


Fig. 5 a The experimental setup. Our BEC is created in an octagonal chamber. Two dipole trap beams (DT1 and DT2) form the crossed dipole trap. The Raman incoming beam is about 7° off-axis from the beam DT2. The incoming Raman beam and the reflected Raman beam are combined with a polarization beam splitter, they are $\sigma+$ at the chamber center. The probe direction is about 45° with respect to the Raman direction

METHODS

The experimental setup is shown in Fig. 5. Two dipole trap (DT) beams are used as the final trap for our BEC. The waist size of the two DT beams is about 70 µm. The trap frequencies of our DT are roughly $\omega = 2\pi \times (90, 90, 90)$ Hz. There are roughly 6×10^4 atoms in our BEC. The Raman beams make roughly a 7° angle with the DT2 beam, and have a size of roughly 230 µm at the position of the BEC. After the chamber, the Raman beam passes through two AOMs and returns to the BEC position.

In order to reduce the momentum spread along Raman direction, we reduce the power of the DT1 laser and increase the Raman beam incoming powers at the same time. The trap frequency along Raman direction becomes about $2\pi \times 40\,\text{Hz}$. The ramp time is 0.4 s and an additional 0.1 s allows for rethermalization of the atoms to avoid breathing or sloshing. The incoming Raman beam is kept on and the intensity is stabilized. The Raman coupling is pulsed on by turning on the two AOMs following the

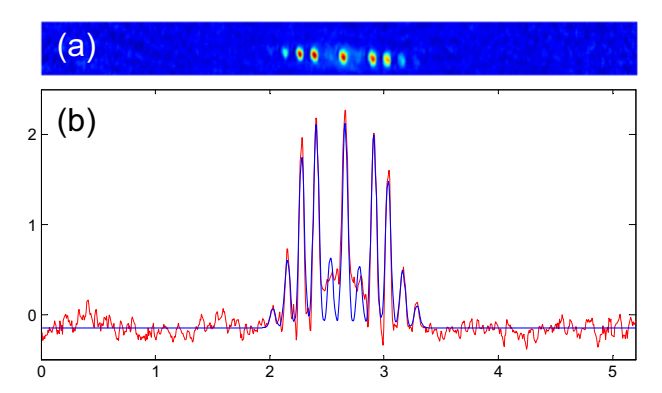


Fig. 6 Detection method. **a** shows the absorption image of atoms with 20-ms free expansion. Atoms in different momentum states occupy different positions after this time-of-flight expansion. These components are very well separated. **b** shows the multi-Gaussian fitting. Each column of the image shown in **a** is summed, and the size of each Gaussian function is set to be equal. As such, the peak values for each column of the fit orders are proportional to the atom numbers belonging to the different momentum orders

BEC and allowing for the retroreflected beam to be turned on, as shown in the left side of Fig. 5.

After the Raman pulse, all the dipole trap beams and the Raman beams are turned off. Atoms fall freely in space. We take an absorption image after 20 ms. At this time, atoms with different momentums will occupy different positions, as shown in Fig. 6a. In order to count the number of atoms in different momentum states, we sum the image along the top–down direction, and then fit it with a multi-Gaussian function. The size of each Gaussian peak is set to be the same, and the distance between the nearest peaks is set to be equal. In such constrained fits, the peak value of each Gaussian function is proportional to the atom number at the different momentum states.

DATA AVAILABILITY

The data sets generated and/or analyzed during this study are available from the corresponding author on reasonable request.

np)

ACKNOWLEDGEMENTS

We acknowledge the support from the National Key R&D Program of China under Grant No. 2018YFA0307200, National Natural Science Foundation of China under Grant No. 91736209, National Natural Science Foundation of China under Grant No. 91636104, Natural Science Foundation of Zhejiang province under Grant No. LZ18A040001, and the Fundamental Research Funds for the Central Universities; B.G. acknowledges support from the National Science Foundation under grant No. 1707731

AUTHOR CONTRIBUTIONS

B.Y. and B.G. proposed the idea. D-Z.X, W.G, and T.X performed the experiment and completed the data analysis. B.Y. supervised the project. All authors contributed to writing of the paper.

ADDITIONAL INFORMATION

Competing interests: The authors declare no competing interests.

Publisher's note: Springer Nature remains neutral with regard to jurisdictional claims in published maps and institutional affiliations.

REFERENCES

- Qi, X.-L. & Zhang, S.-C. Topological insulators and superconductors. Rev. Mod. Phys. 83, 1057–1110 (2011).
- Wang, D. et al. Synthesis of antisymmetric spin exchange interaction and chiral spin clusters in superconducting circuits. Nat. Phys. 15, 382 (2019).
- Wang, B., Chen, T. & Zhang, X. Experimental observation of topologically protected bound states with vanishing chern numbers in a two-dimensional quantum walk. *Phys. Rev. Lett.* 121, 100501 (2018).
- 4. Chen, C. et al. Observation of topologically protected edge states in a photonic two-dimensional quantum walk. *Phys. Rev. Lett.* **121**, 100502 (2018).
- Stuhl, B. K., Lu, H. I., Aycock, L. M., Genkina, D. & Spielman, I. B. Visualizing edge states with an atomic Bose gas in the quantum Hall regime. Science 349, 1514–1517 (2015).
- Goldman, N., Budich, J. C. & Zoller, P. Topological quantum matter with ultracold gases in optical lattices. *Nat. Phys.* 12, 639–645 (2016).
- Meier, E. J., An, F. A. & Gadway, B. Observation of the topological soliton state in the Su-Schrieffer-Heeger model. *Nat. Comm.* 7, 13986 (2016).
- Meier, E. J. et al. Observation of the topological Anderson insulator in disordered atomic wires. Science 362, 929 (2018).
- 9. Cai, H. et al. Experimental observation of momentum-space chiral edge currents in room-temperature atoms. *Phys. Rev. Lett.* **122**, 023601 (2019).
- Xiao, M. et al. Geometric phase and band inversion in periodic acoustic systems. Nat. Phys. 11, 240–244 (2015).
- Peng, Y.-G. et al. Experimental demonstration of anomalous Floquet topological insulator for sound. Nat. Comm. 7, 13368 (2016).
- Ningyuan, J., Owens, C., Sommer, A., Schuster, D. & Simon, J. Time- and siteresolved dynamics in a topological circuit. *Phys. Rev. X* 5, 021031 (2015).
- Zhu, W., Hou, S., Long, Y., Chen, H. & Ren, J. Simulating quantum spin Hall effect in the topological Lieb lattice of a linear circuit network. *Phys. Rev. B* 97, 075310 (2018).
- Jotzu, G. et al. Experimental realization of the topological haldane model with ultracold fermions. Nature 515, 237–240 (2014).
- Becker, C. et al. Ultracold quantum gases in triangular optical lattices. New J. Phys. 12, 065025 (2010).
- Jo, G.-B. et al. Ultracold atoms in a tunable optical kagome lattice. Phys. Rev. Lett. 108, 045305 (2012).
- Wirth, G., Oelschlaeger, M. & Hemmerich, A. Evidence for orbital superfluidity in the P-band of a bipartite optical square lattice. Nat. Phys. 7, 147–153 (2011).
- Xu, Z.-F., You, L., Hemmerich, A. & Liu, W. V. π-flux dirac bosons and topological edge excitations in a bosonic chiral p-wave superfluid. Phys. Rev. Lett. 117, 085301 (2016).
- Lin, Y. J., Jimenez-Garcia, K. & Spielman, I. B. Spin-orbit-coupled Bose-Einstein condensates. *Nature* 471, 83 (2011).

- Wang, P. et al. Spin-orbit coupled degenerate fermi gases. Phys. Rev. Lett. 109, 095301 (2012).
- 21. Wu, Z. et al. Realization of two-dimensional spin-orbit coupling for Bose-Einstein condensates. *Science* **354**, 83–88 (2016).
- Zhang, L., Zhang, L. & Liu, X. Dynamical detection of topological charges. Preprint at arXiv:1807.10782 (2018).
- Wang, C., Zhang, P., Chen, X., Yu, J. & Zhai, H. Scheme to measure the topological number of a chern insulator from quench dynamics. *Phys. Rev. Lett.* 118, 185701 (2017)
- 24. Atala, M. et al. Direct measurement of the Zak phase in topological Bloch bands. *Nat. Phys.* **9**, 795–800 (2013).
- Wang, L., Troyer, M. & Dai, X. Topological charge pumping in a one-dimensional optical lattice. *Phys. Rev. Lett.* 111, 026802 (2013).
- Lohse, M., Schweizer, C., Zilberberg, O., Aidelsburger, M. & Bloch, I. A Thouless quantum pump with ultracold bosonic atoms in an optical superlattice. *Nat. Phys.* 12, 350 (2016).
- Nakajima, S. et al. Topological Thouless pumping of ultracold fermions. *Nat. Phys.* 12, 296 (2016).
- Leder, M. et al. Real-space imaging of a topologically protected edge state with ultracold atoms in an amplitude-chirped optical lattice. *Nat. Comm.* 7, 13112 (2016).
- Gómez-León, A. & Platero, G. Floquet-bloch theory and topology in periodically driven lattices. *Phys. Rev. Lett.* 110, 200403 (2013).
- Dal Lago, V., Atala, M. & Torres, L. E. F. F. Floquet topological transitions in a driven one-dimensional topological insulator. *Phys. Rev. A* 92, 023624 (2015).
- An, F. A., Meier, E. J. & Gadway, B. Engineering a flux-dependent mobility edge in disordered zigzag chains. *Phys. Rev. X* 8, 031045 (2018).
- Perez-Gonzalez, B., Bello, M., Gomez-Leon, A. & Platero, G. Interplay between long-range hopping and disorder in topological systems. *Phys. Rev. B* 99, 035146 (2019).
- 33. Sun, N. & Lim, L.-K. Quantum charge pumps with topological phases in a Creutz ladder. *Phys. Rev. B* **96**, 035139 (2017).
- Jünemann, J. et al. Exploring interacting topological insulators with ultracold atoms: the synthetic creutz-hubbard model. Phys. Rev. X 7, 031057 (2017).
- Maffei, M., Dauphin, A., Cardano, F., Lewenstein, M. & Massignan, P. Topological characterization of chiral models through their long time dynamics. *New J. Phys.* 20, 013023 (2018).
- Lustig, E. et al. Photonic topological insulator in synthetic dimensions. *Nature* 567, 356 (2019).
- Celi, A. et al. Synthetic gauge fields in synthetic dimensions. Phys. Rev. Lett. 112, 043001 (2014).
- 38. Xiao, L. et al. Higher winding number in a nonunitary photonic quantum walk. *Phys. Rev. A* **98**, 063847 (2018).
- 39. Cardano, F. et al. Detection of Zak phases and topological invariants in a chiral quantum walk of twisted photons. *Nat. Comm.* **8**, 15516 (2017).
- 40. Meier, E. J., An, F. A. & Gadway, B. Atom-optics simulator of lattice transport phenomena. *Phys. Rev. A* **93**, 051602 (2016).
- 41. Xie, D., Wang, D., Gou, W., Bu, W. & Yan, B. Fast production of rubidium Bose-Einstein condensate in a dimple trap. J. Opt. Soc. Am. B-Opt. Phys. 35, 500–503 (2018).
- 42. Gadway, B. Atom-optics approach to studying transport phenomena. *Phys. Rev. A* **92**, 043606 (2015).



Open Access This article is licensed under a Creative Commons Attribution 4.0 International License, which permits use, sharing,

adaptation, distribution and reproduction in any medium or format, as long as you give appropriate credit to the original author(s) and the source, provide a link to the Creative Commons license, and indicate if changes were made. The images or other third party material in this article are included in the article's Creative Commons license, unless indicated otherwise in a credit line to the material. If material is not included in the article's Creative Commons license and your intended use is not permitted by statutory regulation or exceeds the permitted use, you will need to obtain permission directly from the copyright holder. To view a copy of this license, visit http://creativecommons.org/licenses/by/4.0/.

© The Author(s) 2019